

ARTICLE

Received 29 Jan 2016 | Accepted 3 May 2016 | Published 2 Jun 2016

DOI: 10.1038/ncomms11811

OPEN

Fluorescence microscopy as an alternative to electron microscopy for microscale dispersion evaluation of organic–inorganic composites

Weijiang Guan¹, Si Wang¹, Chao Lu¹ & Ben Zhong Tang²

Inorganic dispersion is of great importance for actual implementation of advanced properties of organic–inorganic composites. Currently, electron microscopy is the most conventional approach for observing dispersion of inorganic fillers from ultrathin sections of organic–inorganic composites at the nanoscale by professional technicians. However, direct visualization of macrodispersion of inorganic fillers in organic–inorganic composites using high-contrast fluorescent imaging method is hampered. Here we design and synthesize a unique fluorescent surfactant, which combines the properties of the aggregation-induced emission (AIE) and amphiphilicity, to image macrodispersion of montmorillonite and layered double hydroxide fillers in polymer matrix. The proposed fluorescence imaging provides a number of important advantages over electron microscope imaging, and opens a new avenue in the development of direct three-dimensional observation of inorganic filler macrodispersion in organic–inorganic composites.

¹State Key Laboratory of Chemical Resource Engineering, Beijing University of Chemical Technology, 15 Beisanhuan East Road, PO Box 98, Beijing 100029, China. ²Department of Chemistry, Hong Kong Branch of Chinese National Engineering Research Center for Tissue Restoration and Reconstruction, Hong Kong University of Science and Technology, Clear Water Bay, Hong Kong 999077, China. Correspondence and requests for materials should be addressed to C.L. (email: luchao@mail.buct.edu.cn) or to B.Z.T. (email: tangbenz@ust.hk).

Since the birth of organic–inorganic composites, they have undoubtedly been one of the most important and active scientific fields^{1–5}. For such composite materials, the dispersion state of inorganic fillers in organic matrix plays a vital role for attainable improvements of their properties^{6–9}. The dispersion–property relationship can be understood through the direct observation of the spatial distribution of inorganic fillers. The conventional observation method for inorganic filler microdispersion in organic matrix is performed by electron microscopy techniques, such as transmission electron microscopy (TEM) and three-dimensional (3D)-TEM tomography^{6–14}. Notwithstanding the impressive amount of their data on microdispersion of inorganic fillers, they suffer from their own intrinsic limitations. First, the sample preparation is very complex and time-consuming, requiring professional technicians to cut and thin with special care; second, it is only suitable for evaluating nanodispersion scale in a small area window, and thus the obtained results could not be truly representative of macrodispersion of inorganic fillers; in addition, heavy-element staining is required for some poor-contrast components^{10–14}. Therefore, it appears as a crucial need to develop a preparation-free, operation-simple and high-contrast method for visualization of macrodispersion of inorganic fillers.

The ultrafast and non-invasive 3D visualization is one of native functionalities for confocal fluorescence microscopy (CFM)^{15–17}. In principle, CFM would be a powerful method for analyses of inorganic filler macrodispersion and spatial distribution in organic matrix with a large-enough window if the inorganic fillers could emit light. However, the fluorescence quenching usually occurs upon the formation of the fluorophore aggregates in composite materials via π – π stacking interactions^{18,19}. Therefore, the direct visualization of macrodispersion of inorganic fillers in organic–inorganic composites using high-contrast 3D fluorescent imaging method is hampered. Such a limitation of fluorescent labelling should be overcome by means of the aggregation-induced emission (AIE)-active fluorophores, which are generally non-fluorescent in solution but induced emission highly in the aggregated state or solid state^{20–24}.

Herein, we choose a typical organic–inorganic composite, montmorillonite (MMT) polymer composite, to achieve this possibility. In general, the naturally occurring MMT is hydrophilic, and requires organic modification by intercalating cationic surfactants into the interlayer space through ion exchange to form organically compatible^{25–28}. The organo-modified MMT can be well dispersed in polymer matrix with remarkable improvement of material properties, such as increased strength and heat resistance, decreased gas permeability and flammability,

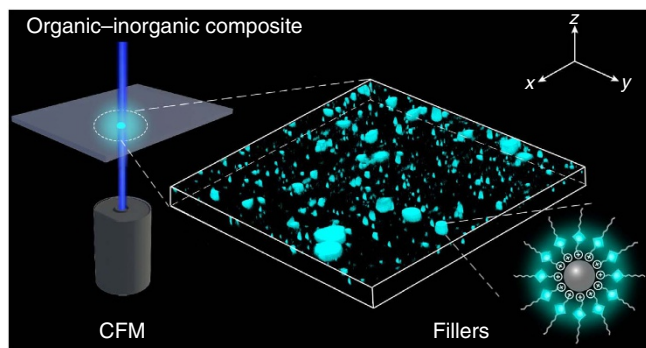


Figure 1 | Schematic representation of visualization of 3D macrodispersion of fillers in organic–inorganic composites. The inorganic fillers modified and bound with AIE molecules are dispersed inside the organic matrix, and then directly visualized by CFM.

and increased biodegradability^{29–33}. It is anticipated that organo-modified MMT can emit light if the intercalated cationic surfactants are attached with an AIE-active fluorophore. In this work, we first synthesize tetraphenylethene (TPE)-cored dodecyltrimethylammonium bromide cationic surfactant (denoted as TPE-DTAB) by incorporating a typical AIE-active TPE luminophore^{34–36} into DTAB. Furthermore, we demonstrate the feasibility of TPE-DTAB as a novel probe for visualization of MMT macrodispersion and spatial distribution in polyvinyl chloride (PVC) matrix with some unique advantages, such as preparation-free, ultrafast and non-invasive (Fig. 1). The generality of the present strategy has also been verified by direct visualization of macrodispersion of layered double hydroxide (LDH) fillers in PVC matrix. This work also serves to demonstrate the general potential in the use of suitable AIE-active luminophores for the visualization of the filler macrodispersion in other organic–inorganic composites.

Results

Characterizations of TPE-DTAB. As depicted in Supplementary Fig. 1, in our synthetic strategy for TPE-DTAB surfactant, we first prepared a fluorescent TPE core with two hydroxyl groups (1, TPE-2OH) to allow access to alkyl chain and alkyl bromide, respectively³⁷. Then TPE-2OH was treated with equivalent moles of NaH to activate a hydroxyl group of TPE-2OH, followed by introducing *n*-octane in one side of TPE-2OH to yield compound 2 (ref. 38). After removal of the unreacted TPE-2OH, the reaction between 1,4-dibromobutane and compound 2 was performed in the presence of alkaline K_2CO_3 to generate bromo-functionalized compound 3 (ref. 39). The molecular structures of the above intermediate compounds were characterized and verified by ¹H nuclear magnetic resonance (NMR) spectroscopy (Supplementary Figs 2–4). Next, the alkyl bromide of compound 3 was converted to the alkyl trimethylamine bromide by adding excess amount of trimethylamine. Finally, TPE-DTAB (4) was successfully synthesized⁴⁰. From the ¹H NMR spectrum of the purified TPE-DTAB (Fig. 2a), the characteristic peaks of TPE were clearly

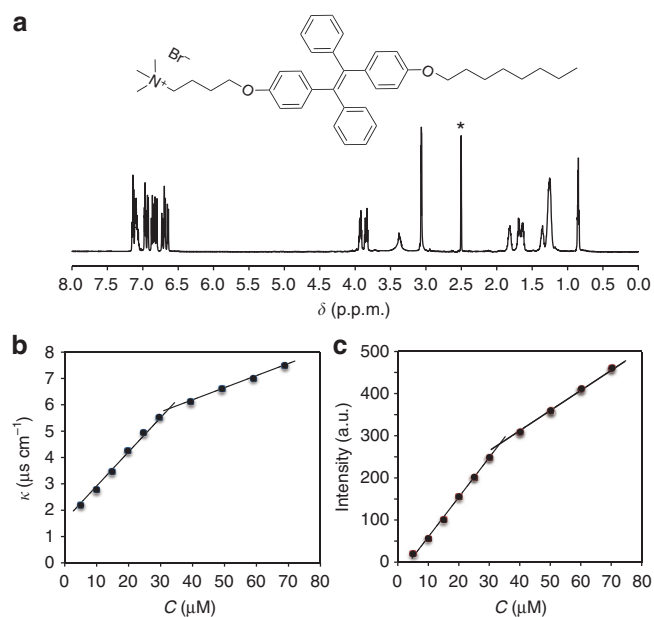


Figure 2 | Molecular structure and characterization of TPE-DTAB.

(a) ¹H NMR spectrum of TPE-DTAB in $[D_6]$ dimethyl sulfoxide (the solvent peak is marked with asterisk). Plots of conductivity (b) and fluorescence intensity at 490 nm (c) versus the concentration of TPE-DTAB. $\lambda_{ex} = 325$ nm.

visible, and the other peaks corresponded nicely to the alkyl protons of DTAB. In addition, in the positive-ion mode mass spectrum (MS; Supplementary Fig. 5), a mass-to-charge (m/z) ratio of 590.3996 was found to be consistent with the exact mass of TPE-DTAB without bromide ion. Finally, in combination with the measurement of the ^{13}C NMR spectrum (Supplementary Fig. 6), we confirmed the structure of the cationic TPE-DTAB.

The critical micelle concentration (CMC) value of the cationic TPE-DTAB surfactant solution was determined by electrical conductivity method^{41–43}. The conductivities (κ) of the TPE-DTAB at different concentrations (C) were plotted in Fig. 2b. At low concentrations, the solution conductivity increased linearly with an increase in the concentration of TPE-DTAB up to $32\ \mu\text{M}$. However, when the TPE-DTAB concentrations were above $32\ \mu\text{M}$, the straight line was observed with a decreased slope. The change of the slope was ascribed to the fact that the ionic micelles have less charge per unit mass than their unimers^{41–43}. The breakpoint at $\sim 32\ \mu\text{M}$ is generally considered to be the CMC of the TPE-DTAB surfactant.

The optical properties of the TPE-DTAB surfactant solution were investigated by measuring its ultraviolet–visible absorption and fluorescence spectra. As shown in Supplementary Fig. 7, two absorption peaks appeared at about 251 and 320 nm, which were attributed to the absorption of benzene and TPE unit⁴⁴. On the other hand, the fluorescence emission wavelength remained at 490 nm, indicative of a typical TPE pattern of light^{34–36,44}. The fluorescence intensity of the TPE-DTAB surfactant solution at 490 nm was plotted as a function of the TPE-DTAB concentration (Fig. 2c). Two straight lines with different slopes in the intensity–concentration plot were found with an inflection point at $\sim 32\ \mu\text{M}$, indicating the changes of the TPE-DTAB morphology⁴⁵. Moreover, ultraviolet absorption and photoluminescence excitation spectra of TPE-DTAB were recorded below and above CMC (Supplementary Fig. 8). It can be seen that absorbance is simply proportional to photoluminescence species. However, inner filter effect could happen if absorbance is higher than 0.05, causing disproportional increasing of photoluminescence intensity with the increase of the concentration of photoluminescence species⁴⁶. Experimentally, we obtained the linear relationship between TPE-DTAB concentration and photoluminescence intensity. The result may be ascribed to the combined effects, including inner filter effect, AIE effect and some other uncertain effects. The resulting CMC value by fluorescence measurement matched well with that obtained from the conductivity measurement, demonstrating that the synthesized TPE-DTAB is a kind of cationic fluorescent surfactant.

Characterizations of TPE-DTAB-modified MMT. It is known that Na^+ -MMT is hydrophilic and well dispersed in polar solvent like water; however, the agglomeration of Na^+ -MMT particles is inevitably occurred when they are mixed with organic polymer matrix to fabricate organic–inorganic composites. To obtain hydrophobic MMT, the TPE-DTAB was intercalated into the interlayer space of Na^+ -MMT via ion exchange method^{25–28}. The X-ray diffraction patterns of Na^+ -MMT and TPE-DTAB-modified MMT were measured to study the structure change of MMT. It is known that 2θ change in the range of 2° – 10° for layered silicates indicated the formation of new ordered intercalated cationic layers^{47–49}. As shown in Fig. 3a, the (001) diffraction peak of Na^+ -MMT occurred at 7.00° , reflecting a d -spacing (d_{001}) of $12.6\ \text{\AA}$. Interestingly, the (001) peak of the TPE-DTAB-modified MMT was shifted to 4.61° and 2.27° , indicating an enlarged d -spacing of 19.2 and $39 \pm 1\ \text{\AA}$, respectively, suggesting that the MMT interlayers might be intercalated with TPE-DTA⁺ ions in different arrangements (Supplementary Fig. 9)^{47–49}.

Fourier transform infrared spectra of the TPE-DTAB, the Na^+ -MMT and the TPE-DTAB-modified MMT further confirmed the combination of the TPE-DTA⁺ ions and the MMT particles (Fig. 3b). In comparison with the Na^+ -MMT, the TPE-DTAB-modified MMT exhibited two new absorption bands at $2,926$ and $2,855\ \text{cm}^{-1}$, which were ascribed to the asymmetrical and symmetrical stretching vibrations of methylene groups in the alkyl chains of TPE-DTAB, respectively⁵⁰. Moreover, the absorption intensity at $3,624\ \text{cm}^{-1}$ of the TPE-DTAB-modified MMT was lower than that of the Na^+ -MMT because of the improved hydrophobicity⁵¹. In conclusions, the TPE-DTA⁺ ions can be inserted into the interlayers of MMT.

On the other hand, the inorganic cations at the external surfaces of MMT particles would be also replaced by TPE-DTA⁺ ions as a result of the ion exchange reaction between TPE-DTAB and Na^+ -MMT. It is known that the adsorption of ionic surfactants at the particle surface usually has a great impact on the ζ potential of the particle^{52–55}. Therefore, to clarify the configuration of TPE-DTAB at the MMT surfaces, we measured the ζ potential of the TPE-DTAB, Na^+ -MMT and TPE-DTAB-modified MMT, respectively (Fig. 3c). The TPE-DTAB showed a positive ζ potential of $43.5\ \text{mV}$, whereas the Na^+ -MMT particles had the negatively charged surfaces with a negative ζ potential of $-28.8\ \text{mV}$. For the TPE-DTAB-modified MMT, its ζ potential was changed to approximately zero, indicating that TPE-DTA⁺ ions were adsorbed at the MMT surface via electrostatic attraction to expose their hydrophobic tails to the aqueous environment⁵⁵. In addition, the Na^+ -MMT particles dispersed well in water; however, the TPE-DTAB-modified MMT particles seemed to be very swollen and hydrophobic. In comparison, the hydrophobic property of TPE-DTAB-modified MMT particles were further confirmed via their good dispersion in petroleum ether (PE) for 24 h (inset of Fig. 3c).

It is essential to study the fluorescence property of TPE-DTAB-modified MMT in the solid state. Figure 3d showed the fluorescence spectra of the Na^+ -MMT powder and the TPE-DTAB-modified MMT powder. The TPE-DTAB-modified MMT powder could emit strong blue–green fluorescence, whereas no fluorescence emissions appeared for the Na^+ -MMT powder. Moreover, the fluorescence quantum yield was significantly enhanced from 5.79% (TPE-DTAB solution) to 42.10% (TPE-DTAB-modified MMT powder), demonstrating that the intramolecular motions of the AIE-active TPE-DTA⁺ ions were tightly restrained by the rigid framework of MMT layers to suppress the non-radiative decay⁵⁶. Therefore, the as-prepared TPE-DTAB-modified MMT powder was endowed not only a hydrophobic property but also an excellent fluorescence-enhanced performance, distinguishing from conventional fluorophores (aggregation-caused quenching effect).

Macrodispersion of MMT in PVC/MMT composite. The PVC/TPE-DTAB-modified MMT (5 wt%) composite was prepared to investigate the macrodispersion of MMT fillers in PVC matrix by TEM and CFM, respectively. TEM image was obtained from the lateral slice of the PVC/TPE-DTAB-modified MMT composite for the morphological characterization and microdispersion of TPE-DTAB-modified MMT particles in PVC matrix (Fig. 4a). However, TEM observation area was not large enough, and the analysis of microdispersion state was usually dependent on the cut cross-section. In contrast, the as-prepared PVC/MMT composite can be directly observed through CFM by means of the strong AIE-active fluorescence emissions of TPE-DTAB-modified MMT particles. As shown in Fig. 4b, the dark background ($600 \times 600\ \mu\text{m}^2$) was dotted with hundreds of luminescent particles to provide a fluorescence distribution map,

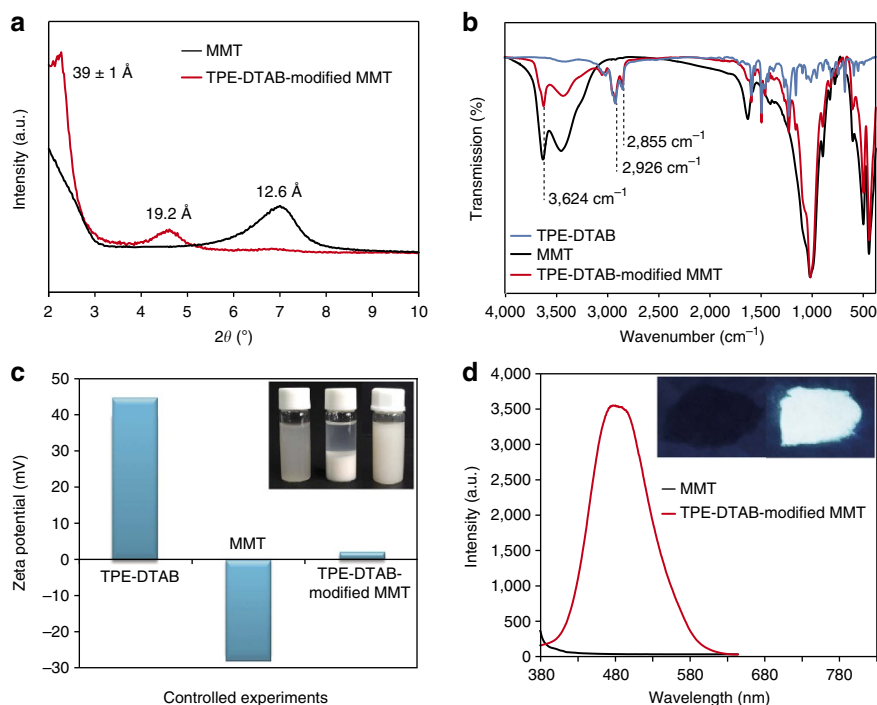


Figure 3 | Characterizations of TPE-DTAB-modified MMT. (a) Powder X-ray diffraction patterns of Na⁺-MMT and TPE-DTAB-modified MMT. (b) Fourier transform infrared spectra of TPE-DTAB, Na⁺-MMT and TPE-DTAB-modified MMT. (c) ζ potential measurements of TPE-DTAB, Na⁺-MMT and TPE-DTAB-modified MMT; the inset showed the photographs of Na⁺-MMT in water, TPE-DTAB-modified MMT in water and TPE-DTAB-modified MMT in petroleum ether for 24 h, respectively. (d) Fluorescence spectra of Na⁺-MMT and TPE-DTAB-modified MMT; the inset showed the photographs of Na⁺-MMT powder (left) and TPE-DTAB-modified MMT powder (right) under ultraviolet irradiation at 365 nm.

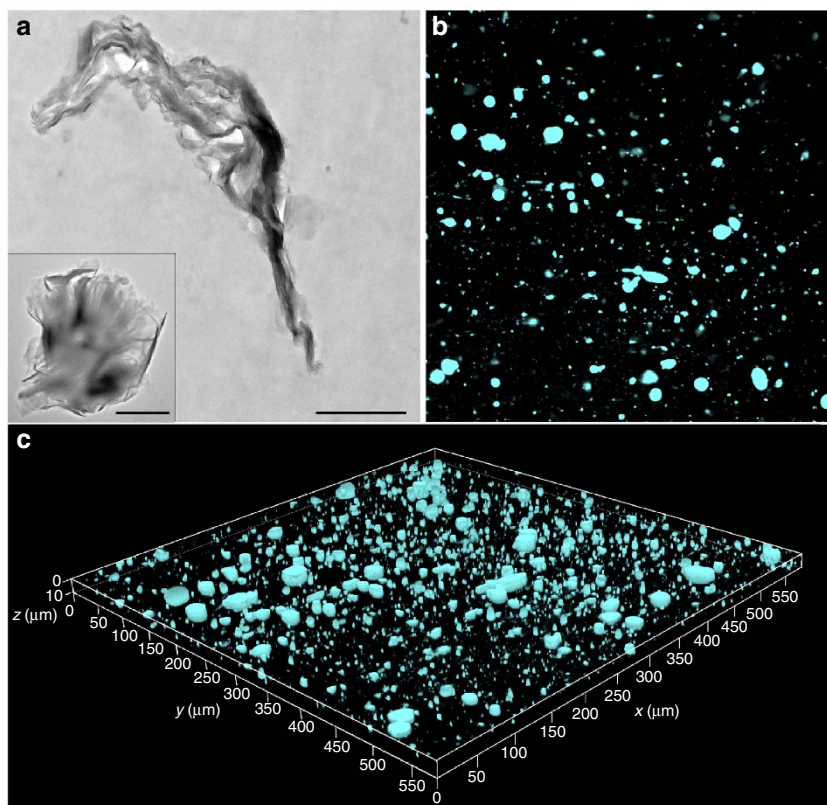


Figure 4 | Macrodispersion of organo-modified MMT in PVC/MMT composite. (a) Cross-sectional TEM micrograph of PVC/TPE-DTAB-modified MMT (5 wt%) composite; the inset showed TEM image of TPE-DTAB-modified MMT. Scale bar, 1 μm. (b) Fluorescence microscopy image (600 × 600 μm²) of PVC/TPE-DTAB-modified MMT (5 wt%) composite. (c) 3D representation of TPE-DTAB-modified MMT dispersion (cyan parts) in PVC matrix. All fluorescence microscopy images were taken with a 405-nm laser.

clearly demonstrating the macrodispersion state (XY plane) of the TPE-DTAB-modified MMT particles in PVC. Furthermore, a total of 30 images in the XY plane were collected at different depths using Z-scan technique. As a result, the spatial distribution of TPE-DTAB-modified MMT particles in PVC matrix was achieved by combining these obtained XY-plane images (Fig. 4c). A large area can be observed in such images, and thus the imaging of the real dispersed state of MMT was captured, facilitating an impartial judgement of the overall dispersion state of the composite material. More importantly, this preparation-free imaging method is very convenient and time saving (~5 s for one picture), similar to an ultrafast and non-invasive computed tomography scan to macrodispersion of the composite material.

On the other hand, the dispersion of TPE-DTAB-modified MMT was compared with that of traditional organoclays. Herein, we incorporated TPE-DTAB as a small percentage of guests in traditional organo-MMT (that is, cetyltrimethyl ammonium bromide (CTAB)-modified MMT). Then, the PVC/CTAB/TPE-DTAB-modified MMT (5 wt%) composite was prepared for dispersion evaluation by CFM. As shown in Supplementary Fig. 10, with the help of the fluorescent TPE-DTAB, we could also directly observe the spatial distribution of CTAB/TPE-DTAB-modified MMT by CFM. In comparison with PVC/TPE-DTAB-modified MMT composite, PVC/CTAB/TPE-DTAB-modified MMT composite exhibited a similar dispersion state, although its fluorescence intensity was much lower as a result of small amounts of TPE-DTAB.

Macrodispersion of LDH in PVC/LDH composite. In addition, another popular organic-inorganic composite, PVC/LDH composite^{57,58}, was also investigated to verify the generality of the developed visualization strategy. Similarly, the positively charged LDHs were organically modified by an AIE-active anionic surfactant (TPE-SDS) to possess both organic compatibility and AIE characteristic. Supplementary Fig. 11 showed the TEM image of the LDH microdispersion in PVC matrix. On the other hand, the spatial distribution of LDHs were also directly visualized by CFM (Supplementary Fig. 12). These results demonstrated that the proposed visualization strategy exhibited the generality for studying the spatial distribution of inorganic fillers in organic matrix.

Discussion

In conclusion, we have synthesized a new fluorescent surfactant with AIE effect through attachment of TPE units onto cationic surfactants. The resulting cationic surfactant TPE-DTAB facilitates the construction of organo-modified MMT in order to be compatible with polymer matrix. Furthermore, the synthesis of TPE-DTAB surfactant enables us to develop a simple and versatile fluorescence imaging platform for direct observation of macrodispersion of MMT fillers in polymer matrix. The generality of this strategy further highlights 3D visualization of LDH filler macrodispersion in PVC matrix. Note that scanning electron microscopy could give microscale imaging with simple sample preparation. However, scanning electron microscopy is usually used for investigating surface topography. With the help of penetration depth of electrons, it might also observe dispersion of particles in slight interior of samples. In comparison to the nanoscale electron microscopy techniques (for example, TEM and 3D-TEM tomography), the AIE-active CFM technology offers the advantages of a wide-view dispersion image with simplicity, sensitivity and high-contrast, but a limited spatial resolution of fine structure by light diffraction (~200 nm in the lateral dimension and 500 nm in the axial dimension)^{15,17}. In contrast, super-resolution microscopy imaging techniques, such

as stimulated emission depletion microscopy and stochastic optical reconstruction microscopy, can obtain a higher resolution than the diffraction limit. For example, stimulated emission depletion microscopy can achieve an image resolution of 20–40 nm in the lateral dimensions and 30–50 nm in the axial dimension¹⁷; while stochastic optical reconstruction microscopy can reach 20–30 nm and 50–60 nm for the lateral resolution and axial resolution, respectively⁵⁹. It is worth mentioning that super-resolution microscopy is potentially applicable to the proposed AIE method if we can synthesize some AIE molecules suitable for such technique. On the other hand, cathodoluminescence by the interaction between electron beams and solid luminescent materials is a similar idea for the proposed AIE method, which has been widely used to investigate the nanoscale properties of solid samples⁶⁰. Specially, the defect structure of solid samples could be visualized by cathodoluminescence microscopy⁶¹, which is difficult for the proposed AIE method. In addition, the proposed AIE molecules in our study are designed for charged inorganic and organic substances, which is inapplicable to non-charged inorganic and organic substances. However, it has been reported that non-charged inorganics could be easily modified by luminescent polymers through physisorption⁶². With these merits in the current protocol, this facile imaging platform may open viable opportunities and inspirations for macrodispersion of other inorganic fillers in organic-inorganic composites, especially for dispersion of composite materials difficult to be distinguished using electron microscope imaging.

Methods

Materials. Zinc dust and 4-hydroxyl benzophenone were purchased from Sigma-Aldrich Chemical Co. Sodium hydride (NaH), TiCl₄, poly(vinyl chloride) with Mn = 67,750 (polydispersity index (PDI) = 2.32), dioctyl phthalate (DOP), CTAB, calcium stearate, zinc stearate, NaCl and K₂CO₃ were purchased from J&K Chemical Ltd. Anhydrous dimethyl formamide (DMF), tetrahydrofuran (THF) and sodium sulfate were purchased from Alfa Aesar. 1-Bromooctane, 1,4-dibromobutane and trimethylamine in THF (100 ml, 1.0 M) were purchased from Tokyo Chemical Industry. Ethanol, PE, acetone, ethyl acetate (EA) and dichloromethane were purchased from Beijing Chemical Reagent Company. Sodium montmorillonite (Na⁺-MMT) with cation exchange capacity values of 145 meq per 100 g (from Nanacor, PGW grades) was used without further purification. Carbonate intercalated Mg-Al LDHs (with a molar ratio of 2:1 between Mg²⁺ and Al³⁺) were synthesized and characterized according to the literature³⁴. TPE-SDS was synthesized and characterized according to our previous work³⁶. All reagents were of analytical grade and used without further purification. Water was purified with a Milli-Q purification system (Milli-Q).

Synthesis of compound 1. In a 250-ml, two-necked, round-bottom flask equipped with a condenser, zinc dust (2.9 g, 44 mmol) and 4-hydroxybenzophenone (2.0 g, 10 mmol) were dissolved in 100 ml dry THF under nitrogen. The mixture was cooled to -78 °C and TiCl₄ (2.5 ml, 22 mmol) was added dropwise. After the addition, the mixture was allowed to warm to room temperature in 0.5 h, and then was heated to reflux for overnight. The reaction was quenched with 10% aqueous K₂CO₃ solution. The mixture was extracted with diethyl ether for three times and the combined organic layer was washed with brine twice and dried over sodium sulfate. After solvent evaporation, the crude product was separated through silica-gel chromatography flushed with PE/EA (v/v 1:1). 1.56 g product was obtained as a white solid with a yield of 86%. ¹H NMR (600 MHz, CDCl₃, δ): 6.94–7.05 (m, 10H), 6.76–6.81 (m, 4H), 6.47–6.52 (m, 4H).

Synthesis of compound 2. Under N₂ atmosphere, sodium hydride (0.022 g, 0.55 mmol) was added to the solution of 1 (0.182 g, 0.50 mmol) in dry DMF (10 ml) and the mixture was stirred for extra 30 min at room temperature. Then 1-bromooctane (0.145 g, 0.75 mmol) was added and the reaction mixture was stirred at 60 °C for 8.0 h. When the reaction completed, the solvent DMF was removed and the residue was redissolved with EA, and the resulting solution was washed with water for three times and dried over sodium sulfate. The solution was concentrated and the residue was purified through silica gel chromatography flushed with PE/EA (7:1 v/v), compound 2 (0.121 g, 0.25 mmol) as a yellow liquid was obtained with a yield of 51%. ¹H NMR (600 MHz, CDCl₃, δ): 6.98–7.11 (m, 10H), 6.83–6.92 (m, 4H), 6.52–6.63 (m, 4H), 3.82–3.88 (m, 2H), 1.67–1.76 (m, 2H), 1.37–1.41 (m, 2H), 1.24–1.29 (m, 8H), 0.85–0.88 (t, 3H).

Synthesis of compound 3. The compound 2 (0.174 g, 0.50 mmol) and K_2CO_3 (0.076 g, 0.55 mmol) were mixed in 20 ml acetone. After stirred for 1 h, 1,4-dibromobutane (0.118 g, 0.55 mmol) was added and the resulting mixture was stirred for 24 h at 60 °C. After evaporation of acetone, the obtained solids were first redispersed in EA and then filtered to remove the insoluble K_2CO_3 . The purified product was obtained in 74% yield after purification separation by silica gel chromatography using PE/EA (10:1 (v/v)). 1H NMR (600 MHz, $CDCl_3$, δ): 7.00–7.12 (m, 10H), 6.88–6.95 (m, 4H), 6.59–6.65 (m, 4H), 4.20–4.25 (m, 2H), 3.84–3.93 (m, 4H), 2.43–2.46 (m, 2H), 1.81–1.86 (m, 4H), 1.70–1.76 (m, 2H), 1.38–1.43 (m, 2H), 1.26–1.32 (m, 8H), 0.87–0.89 (t, 3H).

Synthesis of TPE-DTAB (compound 4). A 100-ml flask with a magnetic spin bar was charged with 3 (0.3 g, 0.50 mmol) dissolved in 20 ml of THF. To this solution, trimethylamine (1.0 M, 5 ml) was added. The mixture was heated to reflux and stirred for 3 days. During this period, 5 ml of trimethylamine in THF was added at several intervals. After THF and extra trimethylamine were evaporated, the residue was washed with chloroform and acetone and then dried overnight *in vacuo* at 60 °C. A yellowish product was obtained in 88% yield. 1H NMR (600 MHz, $DMSO-d_6$, δ): 7.07–7.15 (m, 6H), 6.92–6.98 (m, 4H), 6.80–6.88 (m, 4H), 6.64–6.73 (m, 4H), 3.91–3.95 (m, 2H), 3.82–3.87 (m, 2H), 3.34–3.39 (m, 2H), 3.07–3.09 (t, 9H), 1.79–1.85 (m, 2H), 1.61–1.72 (m, 4H), 1.34–1.36 (m, 2H), 1.24–1.27 (m, 8H), 0.84–0.86 (t, 3H). ^{13}C NMR (600 MHz, $DMSO-d_6$, δ): 157.54, 157.29, 144.27, 144.20, 139.82, 139.64, 136.22, 132.41, 132.36, 131.19, 128.28, 128.17, 126.79, 126.76, 114.23, 114.19, 114.14, 114.09, 67.67, 66.97, 65.40, 52.60, 31.69, 29.20, 29.16, 29.12, 26.11, 26.02, 25.99, 22.55, 19.72, 14.43. MS: *m/z*: 590.3996 ($[M-Br]^+$, calculated for $C_{41}H_{52}NO_2$, 590.3993).

Synthesis of TPE-DTAB-modified MMT and TPE-SDS-modified LDH.

TPE-DTAB-modified MMT was prepared from Na^+ -MMT by ion exchange method. Typically, a 0.5 g portion of Na^+ -MMT was mixed with 50 ml of deionized water. Then, 0.5 g of TPE-DTAB was added in the MMT solution. The ion exchange was carried out under stirring for 1 h at 60 °C. Then, the reaction solution was centrifuged at 5,000 r.p.m. for 5 min, and the precipitate was washed with distilled water to remove the physically adsorbed TPE-DTAB. The obtained TPE-DTAB-modified MMT was dried under vacuum at 60 °C, and then finely powdered in an agate mortar for further use. TPE-SDS-modified LDH powder was prepared according to the same procedure.

Synthesis of CTAB/TPE-DTAB-modified MMT. Na^+ -MMT (0.5 g) was dispersed in 50 ml of deionized water. Then, a mixture of TPE-DTAB (0.05 g) and CTAB (0.25 g) was added to the MMT dispersion and stirred for 1 h at 60 °C. After centrifugation and washing, the obtained CTAB/TPE-DTAB-modified MMT solid was dried under vacuum at 60 °C and ground into powder.

Preparation of PVC/MMT composite. The PVC/TPE-DTAB-modified MMT composite, containing 10.0 g PVC powder, 5.0 g DOP and 0.5 g TPE-DTAB-modified MMT powder, was prepared by blending in a heated double-roller mixer for 5 min at 140 °C. The resulting composites were molded at 120 °C and then cooled at room temperature to give thin films with a thickness of 1 mm. The PVC/CTAB/TPE-DTAB-modified MMT composite was prepared according to the same procedure.

Preparation of PVC/LDH composite. The PVC/TPE-SDS-modified LDH composite, containing 10.0 g PVC powder, 5.0 g DOP, 0.2 g TPE-SDS-modified LDH powder, 0.23 g calcium stearate and 0.1 g zinc stearate, was prepared by blending in a heated double-roller mixer for 5 min at 140 °C. The resulting composite was molded at 120 °C and then cooled at room temperature to give thin films with a thickness of 1 mm.

TEM sample preparation. The composite films were ultrathin-sectioned with a diamond knife at -120 °C using a Leica EM UC6 ultramicrotome. The obtained ultrathin sections were then collected in a trough filled with deionized water and placed on 200-mesh copper grids.

Characterization. Proton and carbon-13 nuclear magnetic resonance (1H NMR and ^{13}C NMR) spectra were recorded at room temperature with a 600-MHz Bruker spectrometer (Bruker). MS was carried out with Quattro microtriple quadrupole mass spectrometer (Waters). Electrical conductivity measurements were performed using a EC 215 conductivity meter (Shanghai Jingmi Instrumental Co.). TEM photographs were performed on a Tecnai G220 TEM (FEI Company) at an accelerating voltage of 200 kV. Ultraviolet-visible spectra were measured on a USB 4000 miniature fibre optic spectrometer in absorbance mode with a DH-2000 deuterium and tungsten halogen light source (Ocean Optics). Fluorescence spectra were obtained using a F-7000 fluorescence spectrophotometer at a slit of 5.0 nm with a scanning rate of $1,200$ nm min^{-1} . X-ray diffraction measurements of MMT and TPE-DTAB-modified MMT were performed with a Bruker D8 ADVANCE X-ray diffractometer (Bruker) equipped with graphite-monochromatized $Cu/K\alpha$

radiation ($\lambda = 0.1541$ nm). The samples as unoriented powders were step-scanned in steps of 0.02° (2θ) in the range of $2-10^\circ$. Fourier transform infrared spectroscopy experiments were carried out on Nicolet 380 system (Thermo) containing a controlled environment chamber equipped with CaF_2 windows. Zeta potential was determined using a Malvern Zetasizer 3000HS nano-granularity analyzer. The quantum yield values were obtained from the reconvolution fit analysis (Edinburgh F980 analysis software) equipped with an integrating sphere. Fluorescence microscope images were recorded on a confocal laser scanning microscope (Leica, TCS SP8).

Data availability. The data that support the findings of this study are available from the corresponding author upon request.

References

- Ziolo, R. F. *et al.* Matrix-mediated synthesis of nanocrystalline $\gamma-Fe_2O_3$: a new optically transparent magnetic material. *Science* **257**, 219–223 (1992).
- Podsiadlo, P. *et al.* Ultrastrong and stiff layered polymer nanocomposites. *Science* **318**, 80–83 (2007).
- Capadona, J. R., Shanmuganathan, K., Tyler, D. J., Rowan, S. J. & Weder, C. Stimuli-responsive polymer nanocomposites inspired by the sea cucumber dermis. *Science* **319**, 1370–1374 (2008).
- Manias, E. Stiffer by design. *Nat. Mater.* **6**, 9–11 (2007).
- Li, Q. *et al.* Flexible high-temperature dielectric materials from polymer nanocomposites. *Nature* **523**, 576–579 (2015).
- Rittigstein, P., Priestley, R. D., Broadbelt, L. J. & Torkelson, J. M. Model polymer nanocomposites provide an understanding of confinement effects in real nanocomposites. *Nat. Mater.* **6**, 278–282 (2007).
- Chandran, S., Begam, N., Padmanabhan, V. & Basu, J. K. Confinement enhances dispersion in nanoparticle-polymer blend films. *Nat. Commun.* **5**, 3697–3706 (2014).
- Mangal, R., Srivastava, S. & Archer, L. A. Phase stability and dynamics of entangled polymer-nanoparticle composites. *Nat. Commun.* **6**, 7198–7207 (2015).
- Suter, J. L., Groen, D. & Coveney, P. V. Chemically specific multiscale modeling of clay-polymer nanocomposites reveals intercalation dynamics, tactoid self-assembly and emergent materials properties. *Adv. Mater.* **27**, 966–984 (2015).
- Giannelis, E. P. Polymer layered silicate nanocomposites. *Adv. Mater.* **8**, 29–35 (1996).
- Balazs, A. C., Emrick, T. & Russell, T. P. Nanoparticle polymer composites: where two small worlds meet. *Science* **314**, 1107–1110 (2006).
- Wang, J., Lin, L., Cheng, Q. & Jiang, L. A strong bio-inspired layered PNIPAM-clay nanocomposite hydrogel. *Angew. Chem. Int. Ed.* **51**, 4676–4680 (2012).
- Ojijo, V. & Ray, S. S. Nano-biocomposites based on synthetic aliphatic polyesters and nanoclay. *Prog. Mater. Sci.* **62**, 1–57 (2014).
- Ray, S. S. Recent trends and future outlooks in the field of clay-containing polymer nanocomposites. *Macromol. Chem. Phys.* **215**, 1162–1179 (2014).
- Weckhuysen, B. M. Chemical imaging of spatial heterogeneities in catalytic solids at different length and time scales. *Angew. Chem. Int. Ed.* **48**, 4910–4943 (2009).
- Ameloot, R. *et al.* Three-dimensional visualization of defects formed during the synthesis of metal-organic frameworks: a fluorescence microscopy study. *Angew. Chem. Int. Ed.* **52**, 401–405 (2013).
- Hell, S. W. Nanoscopy with focused light (Nobel Lecture). *Angew. Chem. Int. Ed.* **54**, 8054–8066 (2015).
- Levitsky, I. & Krivoslykov, S. G. Rational design of a Nile Red/polymer composite film for fluorescence sensing of organophosphonate vapors using hydrogen bond acidic polymers. *Anal. Chem.* **73**, 3441–3448 (2001).
- Cao, X. D., Li, C. M., Bao, H. F., Bao, Q. L. & Dong, H. Fabrication of strongly fluorescent quantum dot-polymer composite in aqueous solution. *Chem. Mater.* **19**, 3773–3779 (2007).
- Hong, Y. N., Lam, J. W. Y. & Tang, B. Z. Aggregation-induced emission. *Chem. Soc. Rev.* **40**, 5361–5388 (2011).
- Hu, R. R., Leung, N. L. C. & Tang, B. Z. AIE macromolecules: syntheses, structures and functionalities. *Chem. Soc. Rev.* **43**, 4494–4562 (2014).
- Mei, J. *et al.* Aggregation-induced emission: the whole is more brilliant than the parts. *Adv. Mater.* **26**, 5429–5479 (2014).
- Kwok, R. T. K., Leung, C. W. T., Lam, J. W. Y. & Tang, B. Z. Biosensing by luminogens with aggregation-induced emission characteristics. *Chem. Soc. Rev.* **44**, 4228–4238 (2015).
- Mei, J., Leung, N. L. C., Kwok, R. T. K., Lam, J. W. Y. & Tang, B. Z. Aggregation-induced emission: together we shine, united we soar. *Chem. Rev.* **115**, 11718–11940 (2015).
- Schmidt, D. F., Clément, F. & Giannelis, E. P. On the origins of silicate dispersion in polysiloxane/layered-silicate nanocomposites. *Adv. Funct. Mater.* **16**, 417–425 (2006).

26. Iijima, M., Kobayakawa, M., Yamazaki, M., Ohta, Y. & Kamiya, H. Anionic surfactant with hydrophobic and hydrophilic chains for nanoparticle dispersion and shape memory polymer nanocomposites. *J. Am. Chem. Soc.* **131**, 16342–16343 (2009).
27. Maheshwari, S. *et al.* Layer structure preservation during swelling, pillaring, and exfoliation of a zeolite precursor. *J. Am. Chem. Soc.* **130**, 1507–1516 (2008).
28. Schmidt, D. F. & Giannelis, E. P. Silicate dispersion and mechanical reinforcement in polysiloxane/layered silicate nanocomposites. *Chem. Mater.* **22**, 167–174 (2010).
29. Mark, J. E. Some novel polymeric nanocomposites. *Acc. Chem. Res.* **39**, 881–888 (2006).
30. Gilman, J. W. *et al.* Polymer/layered silicate nanocomposites from thermally stable trialkylimidazolium-treated montmorillonite. *Chem. Mater.* **14**, 3776–3785 (2002).
31. Möller, M. W. *et al.* UV-cured, flexible, and transparent nanocomposite coating with remarkable oxygen barrier. *Adv. Mater.* **24**, 2142–2147 (2012).
32. Dang, Z.-M., Yuan, J.-K., Yao, S.-H. & Liao, R.-J. Flexible nanodielectric materials with high permittivity for power energy storage. *Adv. Mater.* **25**, 6334–6365 (2013).
33. Dawson, J. I. & Oreffo, R. O. C. Clay: new opportunities for tissue regeneration and biomaterial design. *Adv. Mater.* **25**, 4069–4086 (2013).
34. Wang, J. *et al.* Click synthesis, aggregation-induced emission, E/Z isomerization, self-organization, and multiple chromisms of pure stereoisomers of a tetraphenylethene-cored luminogen. *J. Am. Chem. Soc.* **134**, 9956–9966 (2012).
35. Li, J. W. *et al.* An aggregation-induced-emission platform for direct visualization of interfacial dynamic self-assembly. *Angew. Chem. Int. Ed.* **53**, 13518–13522 (2014).
36. Guan, W. J., Zhou, W. J., Lu, C. & Tang, B. Z. Synthesis and design of aggregation-induced emission surfactants: direct observation of micelle transitions and microemulsion droplets. *Angew. Chem. Int. Ed.* **54**, 15160–15165 (2015).
37. Yu, C. M. *et al.* Hyperbranched polyester-based fluorescent probe for histone deacetylase via aggregation-induced emission. *Biomacromolecules* **14**, 4507–4514 (2013).
38. Gu, X. *et al.* Polymorphism-dependent emission for di(p-methoxyphenyl) dibenzofulvene and analogues: optical waveguide/amplified spontaneous emission behaviors. *Adv. Funct. Mater.* **22**, 4862–4872 (2012).
39. Xu, X. *et al.* Functionalization of graphene by tetraphenylethylene using nitrene chemistry. *RSC Adv.* **2**, 7042–7047 (2012).
40. Jiang, B.-P., Guo, D.-S., Liu, Y.-C., Wang, K.-P. & Liu, Y. Photomodulated fluorescence of supramolecular assemblies of sulfonatocalixarenes and tetraphenylethene. *ACS Nano* **8**, 1609–1618 (2014).
41. Rosen, M. J. & Kunjappu, J. T. *Surfactants and Interfacial Phenomena* (Wiley, 2012).
42. Holmberg, K., Jönsson, B., Kronberg, B. & Lindman, B. *Surfactants and Polymers in Aqueous Solution* (Wiley, 2002).
43. Shi, L., Lundberg, D., Musaev, D. G. & Menger, F. M. [12]Annulene gemini surfactants: structure and self-assembly. *Angew. Chem. Int. Ed.* **46**, 5889–5891 (2007).
44. Tong, H. *et al.* Protein detection and quantitation by tetraphenylethene-based fluorescent probes with aggregation-induced emission characteristics. *J. Phys. Chem. B* **111**, 11817–11823 (2007).
45. Xia, Y. J. *et al.* Water-soluble nano-fluorogens fabricated by self-assembly of bolaamphiphiles bearing AIE moieties: towards application in cell imaging. *J. Mater. Chem. B* **3**, 491–497 (2015).
46. Lakowicz, J. R. *Principles of Fluorescence Spectroscopy* (Springer, 2006).
47. Mariott, W. R. & Chen, E. Y.-X. Stereochemically controlled PMMA-exfoliated silicate nanocomposites using intergallery-anchored metalocenium cations. *J. Am. Chem. Soc.* **125**, 15726–15727 (2003).
48. Xu, L. *et al.* Interfacial modification of magnetic montmorillonite (MMT) using covalently assembled LbL multilayers. *J. Phys. Chem. C* **118**, 20357–20362 (2014).
49. Pirillo, S., Luna, C. R., López-Corral, I., Juan, A. & Avena, M. J. Geometrical and electronic properties of hydrated sodium montmorillonite and tetracycline montmorillonite from DFT calculations. *J. Phys. Chem. C* **119**, 16082–16088 (2015).
50. Liyanage, A. U., Ikhuoria, E. U., Adenuga, A. A., Remcho, V. T. & Lerner, M. M. Synthesis and characterization of low-generation polyamidoamine (PAMAM) dendrimer–sodium montmorillonite (Na-MMT) clay nanocomposites. *Inorg. Chem.* **52**, 4603–4610 (2013).
51. Gu, Z., Gao, M., Lu, L., Liu, Y. & Yang, S. Montmorillonite functionalized with zwitterionic surfactant as a highly efficient adsorbent for herbicides. *Ind. Eng. Chem. Res.* **54**, 4947–4955 (2015).
52. Lotya, M. *et al.* Liquid phase production of graphene by exfoliation of graphite in surfactant/water solutions. *J. Am. Chem. Soc.* **131**, 3611–3620 (2009).
53. Lin, S. C., Shih, C.-J., Strano, M. S. & Blankschtein, D. Molecular insights into the surface morphology, layering structure, and aggregation kinetics of surfactant-stabilized graphene dispersions. *J. Am. Chem. Soc.* **133**, 12810–12823 (2011).
54. Guan, W. J., Zhou, W. J., Huang, Q. W. & Lu, C. Chemiluminescence as a novel indicator for interactions of surfactant–polymer mixtures at the surface of layered double hydroxides. *J. Phys. Chem. C* **118**, 2792–2798 (2014).
55. Chen, S., Zhou, W. J., Cao, Y. Q., Xue, C. C. & Lu, C. Organo-modified montmorillonite enhanced chemiluminescence via inactivation of halide counterions in a micellar solution. *J. Phys. Chem. C* **118**, 2851–2856 (2014).
56. Guan, W. J., Lu, J., Zhou, W. J. & Lu, C. Aggregation-induced emission molecules in layered matrices for two-color luminescence films. *Chem. Commun.* **50**, 11895–11898 (2014).
57. Liu, J., Chen, G. M. & Yang, J. P. Preparation and characterization of poly(vinyl chloride)/layered double hydroxide nanocomposites with enhanced thermal stability. *Polymer* **49**, 3923–3927 (2008).
58. Awad, W. H. *et al.* Material properties of nanoclay PVC composites. *Polymer* **50**, 1857–1867 (2009).
59. Huang, B., Wang, W., Bates, M. & Zhuang, X. W. Three-dimensional super-resolution imaging by stochastic optical reconstruction microscopy. *Science* **319**, 810–813 (2008).
60. Bischak, C. G. *et al.* Cathodoluminescence-activated nanoimaging: noninvasive near-field optical microscopy in an electron microscope. *Nano Lett.* **15**, 3383–3390 (2015).
61. Götze, J. Application of cathodoluminescence microscopy and spectroscopy in geosciences. *Microsc. Microanal.* **18**, 1270–1284 (2012).
62. Nakao, A. & Fujiki, M. Visualizing spontaneous physisorption of non-charged π -conjugated polymers onto neutral surfaces of spherical silica in nonpolar solvents. *Polym. J.* **47**, 434–442 (2015).

Acknowledgements

This work was supported by National Basic Research Program of China (973 Program, 2014CB932103), the National Natural Science Foundation of China (21575010 and 21375006), Innovation and Promotion Project of Beijing University of Chemical Technology and the Innovation and Technology Commission (ITC-CNERC14SC01).

Author contributions

W.J.G. and C.L. conceived the experiments. W.J.G. and S.W. carried out the experiments. W.J.G., C.L. and B.Z.T. contributed to data analysis and writing of this manuscript.

Additional information

Supplementary Information accompanies this paper at <http://www.nature.com/naturecommunications>

Competing financial interests: The authors declare no competing financial interests.

Reprints and permission information is available online at <http://npg.nature.com/reprintsandpermissions/>

How to cite this article: Guan, W. *et al.* Fluorescence microscopy as an alternative to electron microscopy for microscale dispersion evaluation of organic–inorganic composites. *Nat. Commun.* **7**:11811 doi: 10.1038/ncomms11811 (2016).



This work is licensed under a Creative Commons Attribution 4.0 International License. The images or other third party material in this article are included in the article's Creative Commons license, unless indicated otherwise in the credit line; if the material is not included under the Creative Commons license, users will need to obtain permission from the license holder to reproduce the material. To view a copy of this license, visit <http://creativecommons.org/licenses/by/4.0/>